PHYSICAL REVIEW B VOLUME 40, NUMBER 10 1 OCTOBER 1989

Third sound on patterned substrates. I. Periodic and quasiperiodic arrays

D. T. Smith,* C. P. Lorenson,† and R. B. Hallock
Laboratory for Low Temperature Physics, Department of Physics and Astronomy, University of Massachusetts, Amherst, Massachusetts 01003

(Received 27 February 1989)

An experimental arrangement is described which allows the study of the propagation of classical waves on substrates which can be patterned so as to present the waves with scattering sites. Helium films adsorbed on silicon substrates allow the propagation of third-sound waves whose velocity depends on both the film thickness and the local surface structure of the substrate. Detailed studies are presented for substrates which have been patterned in one dimension with periodic arrays. Band structure and perturbing effects due to imperfections in the structure and position of the scattering sites are seen on the periodic substrate. Quasiperiodic arrays are seen to have a more complicated propagation structure.

I. INTRODUCTION

The propagation of waves in periodic structures[1] has played a profound role in the development of our understanding of a host of phenomena and numerous devices including electron transport in crystal lattices, x-ray scattering, particle accelerators, antennas, etc. In recent years attention has turned to the situation in which some degree of disorder is present in the otherwise periodic structure. For example, Anderson[2] considered the effect of deviations from perfect order in the case of electron propagation in a crystal lattice and discovered that such deviations could have a major effect on the properties of the electron wave functions.

In an effort to study the propagation of classical waves in a convenient context, we have developed experiments which utilize thin films of superfluid helium adsorbed on substrates. Classical waves known as third sound[3] propagate along these films and the waves can be made to interact with scattering centers positioned on the substrates. Changes in the film thickness alter the strength of the scatterers and thus the properties of the scattering can be changed readily during the course of the experiments. In our studies[4] the scatterers are positioned along the substrate so as to present the propagating wave with periodic, quasiperiodic, or random one-dimensional arrays of scatterers. In the work we report here, we describe experiments with periodic and quasiperiodic arrays; in a separate paper[5] we treat the case of random scatterers. Below, we begin in Sec. II with a discussion of the helium film environment and the basic properties of third sound. In Sec. III we describe the apparatus and our techniques. Results and analysis are presented in Sec. IV.

II. HELIUM FILMS AND THIRD SOUND

If ^{4}He atoms are added to an evacuated chamber, or sample cell, at low temperature, some fraction of those atoms will adsorb on the surfaces in the chamber so as to form a film and some will remain in the gas phase. If enough atoms are added to allow a puddle of bulk helium to form on the bottom of the sample cell, the system is said to be saturated and the film, in equilibrium with both vapor at pressure P_0 and bulk helium, is termed a saturated film. In this work we deal entirely with unsaturated films, which are films in equilibrium with vapor at pressures $P < P_0$ so that no bulk helium exists in the cell. The unsaturated films studied here are quite uniform on smooth surfaces because they are thin enough that the helium-substrate interaction dominates over gravity.

The force of attraction between a helium atom and a substrate is the induced dipole-dipole interaction, first proposed by London[6] to explain the van der Waals deviations of gases from ideal-gas behavior. For the case of a helium atom near a (planar) substrate, the attractive potential μ seen by the helium atom can be obtained by integrating the force[7] f over the substrate, thus, one obtains

$$\mu = -\frac{\alpha\beta}{d^3(d+\beta)} \tag{1}$$

with

$$f = \frac{\partial\mu}{\partial d} = \frac{\alpha\beta(3\beta+4d)}{d^4(d+\beta)^2}\ , \tag{2}$$

where α is the van der Waals constant, β is a parameter which quantifies retardation effects,[3] and d is the distance between an helium atom and the substrate. If one is considering an atom on the surface of a film, d corresponds to the helium film thickness. For small d ($d \ll \beta$), the above equations reduce to

$$\mu \simeq \frac{\alpha}{d^3} \tag{3}$$

and

$$f \simeq \frac{3\alpha}{d^4}\ . \tag{4}$$

Because an atom on the surface of a film of thickness d

is in equilibrium with helium vapor, a relationship can be written between d and the cell pressure P by equating the ideal-gas chemical potential with the van der Waals potential, in units of K (atomic layers),[3] seen by an atom on the film surface

$$d^3(1+d/\beta)=\frac{\alpha}{T\ln(P_0/P)}\ , \tag{5}$$

which, for $d \ll \beta$, can be simplified to

$$d^3 \simeq \frac{\alpha}{T\ln(P_0/P)}\ . \tag{6}$$

The existence of a *superfluid* film on a substrate allows a long-wavelength disturbance to propagate on the superfluid film. The sound mode, termed third sound[8] and first observed by Everitt *et al.*,[9] is a long-wavelength (relative to d) thickness and temperature fluctuation in the film caused by motion of the superfluid density ρ_s parallel to the substrate. Brooks *et al.*[10] were able to measure the ratio of the thickness fluctuation to the temperature fluctuation for third sound and found it to be $\Delta d/\Delta T \approx 10^{-3}$ nm/μK at 1.35 K for an intermediate film thickness ($d \simeq 10$ atomic layers), in reasonable agreement with the theory of Bergman.[11] Typical values for ΔT and Δd were observed to be $\Delta T \sim 20$ μK and $\Delta d \sim 0.02$ nm.

Because $\lambda \gg d$, third sound is analogous to tidal or shallow water waves; the velocity C depends, to first order, only the product of the fluid depth and the restoring force per unit mass for the fluid surface: $C=\sqrt{fd}$. For shallow water waves, the restoring force seen by the fluid surface is simply gravity; for third sound the restoring force is the van der Waals attraction, as given in Eq. (2). The third-sound velocity also includes a factor of $\langle \rho_s \rangle/\rho$, where $\langle \rho_s \rangle$ is the average[12] superfluid density in the film and a small but significant[13] temperature-dependent term

$$C^2=\frac{\langle \rho_s \rangle}{\rho}\left[1+\frac{TS}{L}\right]^2 \frac{\alpha\beta(3\beta+4d)}{d^3(d+\beta)^2}\ , \tag{7}$$

where S is the entropy and L the latent heat of the film. For most situations the film superfluid density can be adequately described[12] by

$$\frac{\langle \rho_s \rangle}{\rho}=\frac{\rho_s}{\rho}\left[1-\frac{D(T)}{d}\right]\ , \tag{8}$$

where $D(T)$ is a parameter given by

$$D(T)=a+bT\frac{\rho}{\rho_s}\ , \tag{9}$$

where ρ_s/ρ is the bulk superfluid fraction and where $a=0.5$ layers and $b=1.13$ layers/K for third sound on glass.[12] For[13] $d \ll \beta$

$$C^2 \simeq \frac{\rho_s}{\rho}\left[1+\frac{D(T)}{d}\right]\left[1+\frac{TS}{L}\right]^2 \frac{3\alpha}{d^3}\ . \tag{10}$$

In the discussion of film adsorption and third sound above, it was assumed that the substrate to which the ^{4}He film adsorbed was an ideally flat surface. This, of course, is not the case for actual experimental substrates, which can have roughness over a wide range of length scales. In the presence of surface structure (i.e., local curvature) the surface tension, which acts to minimize the surface area and surface energy, becomes important in determining the film profile.

The condition for equilibrium for the film surface at any point is that the chemical potential μ_c of the film be the same everywhere; μ_c is the sum of a van der Waals term, μ_w, and a surface-energy term

$$\mu_c=\mu_w+\frac{\sigma}{\rho}\left[\frac{1}{R_1}+\frac{1}{R_2}\right]\ . \tag{11}$$

Here σ is the surface tension for liquid helium, ρ is the helium density, and R_1 and R_2 are the radii of the curvature of the film measured in two orthogonal directions. Film profiles have been calculated numerically for several simple systems, including the exposed junction between two materials with different van der Waals constants,[14] a right-angle step in a homogeneous substrate,[15] a film adsorbed on the interior surface of cylindrical pore,[16] and a film adsorbed on the interior surface of a cone.[17]

In the case of a randomly roughened substrate, as might be created by abrading or depositing[18] small particles on a smooth substrate, one might expect to observe a reduced third-sound velocity simply because of the longer path which the third sound must follow. This effect is, in fact, observed experimentally[18,19] in systems of this type at small film coverages; however, as the film thickness is increased, the amount of excess fluid, ΔV, present on the surface can increase dramatically as concave regions begin to fill with fluid. The effect of ΔV on third sound has been studied theoretically by Cohen, Guyer, and Machta[20] (CGM). They find that in the limit where the wavelength is much longer than the length scale of the surface structure, and in the absence of tortuosity, the velocity on the rough substrate, C_r is related to the velocity on a smooth (flat) substrate C_s by

$$C_r=C_s\left[1+\zeta\frac{\partial \Delta V}{\partial d}\right]^{-1/2}\ , \tag{12}$$

where ζ is the density of surface irregularities per unit of macroscopic substrate surface area, and d refers to the film thickness on the smooth substrate. As a function of film thickness, significant amounts of fluid can condense on the rough substrate in a highly nonlinear fashion, making it possible for $\partial(\Delta V)/\partial d$ to become quite large[21] with the result that $C_r \ll C_s$.

III. APPARATUS AND TECHNIQUES

The experiments were carried out in a pumped-bath ^{4}He dewar which could achieve stable temperature regulation in the range $1.25 \le T \le 2$ K. Short-term (≤ 1 h) temperature stability was typically better than 1 mK, although temperature drifts of 5 mK or more were common on time scales of 12–24 h, and were correlated to drifts in room temperature and changes in the helium bath level. Although a high level of temperature stability was demonstrably unnecessary for this work, when data were being collected the temperature was held stable to within ±1 mK.

The sample cell was a brass can with a 7.62 cm inside diameter and a 10.2 cm inside height mounted on a cryostat insert of standard stainless-steel tubing construction. The thermometers were standard Allen-Bradley carbon resistors in compensated ac resistance bridges. The power dissipated in making the resistance measurements was approximately 1 nW; the resistance was independent of the power dissipated for powers less than ~ 10 nW. A small saturated vapor, P_0, cell was located in the helium bath in good thermal contact with the experimental system and the cell thermometers; measurements of the saturated ^{4}He pressure in the P_0 cell made with a Baratron (145BH) pressure gauge[22] were used to calibrate the resistors.

Before an experiment was cooled, the sample cell was evacuated to a pressure $P \leq 10^{-6}$ torr at room temperature and tested for leaks, then flushed several times with helium and evacuated again. The helium films to be studied were created by adding helium atoms to the cell at low temperature via a fill line. Because the cell pressure in the experimental chamber P_c is typically only slightly below saturated vapor pressure for the case of the helium films which we studied, the actual pressure measurement made was a differential measurement between the sample cell and the P_0 cell using a differential pressure gauge. This pressure difference, $\Delta P = P_0 - P_c$, along with the saturated vapor pressure, was then used to determine the film thickness. The pressure measurement is particularly good for determining the film thickness for low coverages ($d \leq 5$ layers) because $\Delta P \geq 0.1$ torr. However, at higher coverages ($d \geq 15$ layers), $\Delta P \leq 0.005$ torr and small errors in pressure measurement can cause large errors in the calculated film thickness. Third-sound measurements on smooth-glass substrates are the most convenient method for monitoring changes in the film thickness in this $d \geq 15$ layers limit. At intermediate coverages, either method is acceptable, and when used simultaneously the two were typically in good agreement. To make the film thickness less sensitive to small changes in the number of atoms in the sample cell, the cell contained a reservoir of packed alumina powder with grain sizes of 0.3, 1.0, or 4.0 μm. Typically, about 5 cm^3 of powder was used, providing at least 1 m^2 of surface area.

Since the temperature fluctuations associated with third sound are small ($\Delta T \simeq 20$ μK for $T \simeq 1.4$ K), a sensitive thermometer, such as a superconducting transition edge bolometer, is required to detect them. For the temperature range of interest, $1.2 \leq T \leq 1.8$ K, aluminum is a good choice of material; bulk Al has a T_c of 1.18 K, but when Al is deposited as a narrow thin film, T_c can be readily enhanced to ≤ 2.0 K. For such films, T_c can be tuned by the application of a modest bias current or magnetic field. Third- sound generators were either made of silver or aluminum. The use of Al generators has the important advantage that any Al thin film can be used interchangeably as a third-sound generator or detector while an experiment is in progress.

The most straightforward way to measure the third-sound velocity is to place a third-sound driver and detector 0.25–1.00 cm apart on a substrate and propagate a third-sound pulse from the driver to the detector, measuring the time of flight. The instrumentation for making such a time-of-flight (TOF) measurement is shown in Fig. 1. The drive pulses typically were zero-offset, clamped, single-cycle sine waves with equivalent frequencies in the range 1–100 kHz, at a repetition rate of $\sim$20–25 Hz. The energy in each pulse was typically in the range 0.1–10 nJ. The current used to bias the Al bolometers was in the range 50–200 μA; the third-sound velocity was independent of bias current over this range. Because of the small drive energies and the modest bias currents used, the direct signal from the Al bolometer was often too weak to clearly show the received third-sound pulse amid the noise. Under these conditions, it was necessary to digitize each detected pulse and signal average the (typically 500) pulses.

In addition to using the pulsed time-of-flight technique, it is useful to be able to drive with a continuous sine wave of a given frequency and detect the magnitude and phase of the received third-sound signal. The electronics used to make such cw measurements is illustrated in Fig. 2. The received third-sound signal is fed to a lock-in amplifier which is interfaced to a computer. A function generator was the source of the drive frequency, f; the lock-in amplifier was used in the "$2f$" mode because the third sound, responding to the drive power, was at frequency $2f$. A superconducting-strip bolometer rapidly looses efficiency when the wavelength of the third sound becomes comparable to or smaller than the width of the bolometer.

Previous work with etched silicon[17] showed clearly that a silicon surface could be roughened to produce a region on which third sound would travel at a much reduced velocity compared to the velocity on a smooth surface. The fact that the index of refraction, $n = C_s / C_r$ could be varied over a broad range ($1 \leq n \leq 6$) by varying the helium film thickness was particularly encouraging,

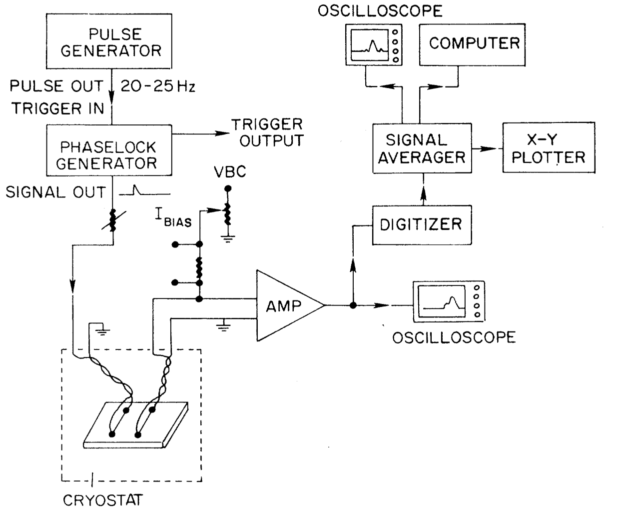

FIG. 1. Schematic illustration of the electronics used to drive and detect pulsed third sound.

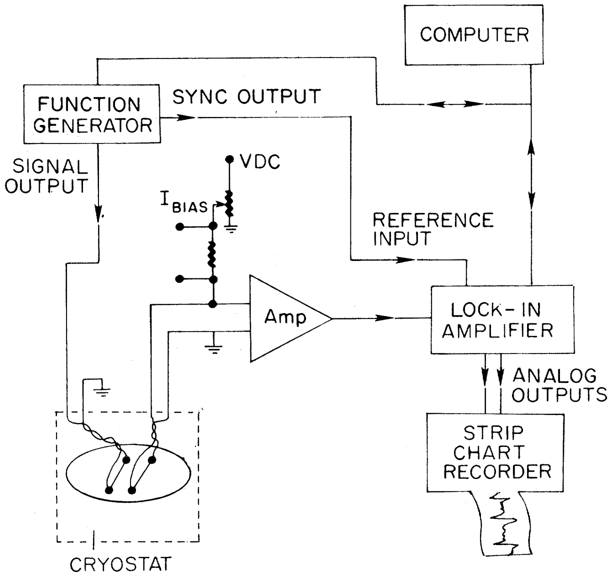

FIG. 2. Schematic illustration of the electronics used to drive and detect continuous-wave third sound.

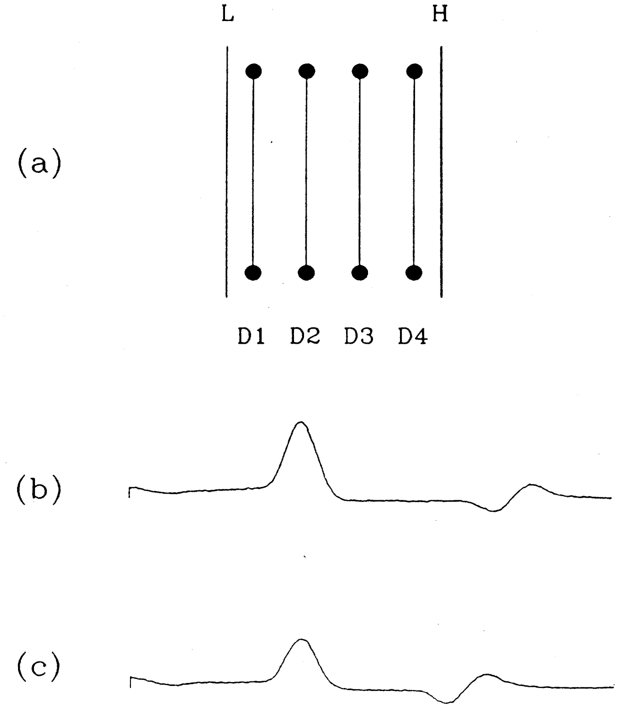

FIG. 3. Experimental arrangement and typical results for the measurement of pulse reflections. (a) Schematic representation of the substrate arrangement used for the measurement of pulse reflections from a light (L) and a heavy (H) scribed channel. $D1$–$D4$ are Al driver-detector thin films. (b) A direct and reflected [from (L)] pulse seen at $D1$ for a drive pulse created at $D2$. (c) A direct and a reflected [from (H)] pulse seen at $D4$ for a drive at $D3$. Note that the detectors $D1$ and $D4$ do not have equal sensitivity.

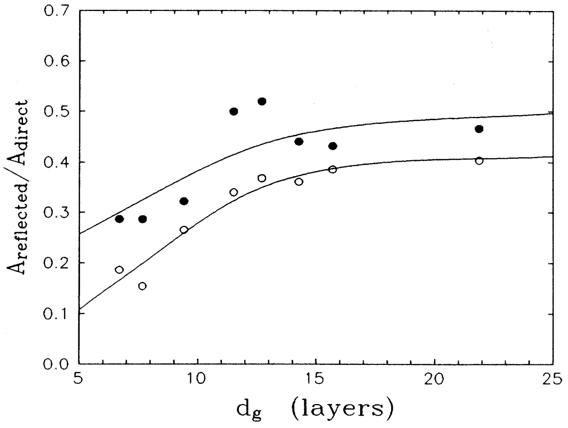

FIG. 4. A simple measure of the scattering power of the light and a heavy scratch as a function of the helium film thickness. Shown here is the ratio of the amplitude of the reflected to the direct pulse for the light (open circles) and heavy (solid circles) scratches. The smooth curves are guides to the eye. d_g is the film thickness measured on a glass thickness-monitor substrate.

because it implied that rough-scattering regions on a smooth substrate could be "tuned" in strength. Work by Generazio and Reed[15] showed that third-sound reflections could be observed from a variety of surface defects in glass, including scribed channels and etched microcracks. It was decided to pursue the possibility of creating scattering arrays by scribing rough channels on an otherwise smooth silicon substrate. A carbide-tipped scribe was used to make scratches on smooth silicon wafers[23] by mounting the scribe in a spring-loaded holder attached to a vertical milling machine head and moving the substrate beneath it with the milling machine table. The force applied between the scribe tip and substrate could be controlled (and reproduced) by noting the spring compression.

To study how scribed channels in silicon interact with a third-sound wave, a silicon substrate was prepared with four Al strips and two scribed channels as shown in Fig. 3(a). The Al strips were 2.54-cm long and spaced every 0.635 cm. One channel (L) was made with relatively low scribe pressure, the other (H) was made with a higher pressure which produced a noticeably heavier scratch. The spacing between L and $D1$ and between H and $D4$ was ~ 0.32 cm. Third-sound pulses were then propagated toward a channel by, for example, driving a pulse with $D2$ while detecting with $D1$. Figure 3(b) shows the received signal at $D1$ triggered at the peak of a 5-kHz drive pulse applied to $D2$; the direct received pulse and the reflection from channel L are clearly visible. Figure 3(c) shows similar data taken by pulsing $D3$ and detecting with $D4$. Although the amplitudes of the two traces are arbitrary, by comparing each reflected pulse to the direct pulse on the same trace it is apparent that the heavier scratch does, in fact, create a stronger reflection.

Data for 5-kHz pulses over a range of film thickness values[24] are shown in Fig. 4 for both the light and heavy scratches; the quantity plotted is the ratio of the inverted reflected pulse height to the direct pulse height. This technique does not accurately determine a true reflection coefficient for several reasons. First, the reflected pulse appears to be a combination of inverted and noninverted parts; a simple measure of pulse height does not correctly determine the amount of reflected energy. Second, third sound attenuates measurably over the distances involved at this temperature; even if a pulse were 100% reflected, the height of the reflected pulse would still not equal the height of the direct pulse because of the longer path taken by the reflected pulse. Nonetheless, observed reflections like those in Figs. 3(b) and 3(c) show qualitatively that third sound does interact with and reflect from scribed channels in silicon with sufficient strength and thickness dependence to indicate that a scribed-channel array is a reasonable candidate for a one-dimensional scattering experiment.

It was decided to use light pressure when making the channel arrays because $A_{\text{reflected}}/A_{\text{direct}}$ for the lighter scratch was small at low coverage; the index of refraction could thus be varied over a larger range than would be possible for heavier scratches. Figure 5 shows a scanning electron microscopy (SEM) picture of a scratch in a silicon wafer taken at an angle of 75° to the normal of the smooth surface on which the scratch was made, showing the depth of the scratch in cross section. Note that the scratch is quite shallow compared to its width, and that its interior region shows quite a bit of rough surface structure.

The first experimental run[4] consisted of two scribed-channel arrays, one with the channels spaced evenly and one with the channels placed at random. A second experiment was performed which compared a (second) periodic array to a quasiperiodic array. Finally, a third experiment was performed which compared both a periodic and a random array to a smooth wafer with no channels so as to study the third-sound modes of the wafer as a whole and to study the effects of ordinary third-sound attenuation on the third-sound propagation. In this paper we report the results for the periodic and quasiperiodic arrays. In a subsequent paper[5] we will report results for random arrays.

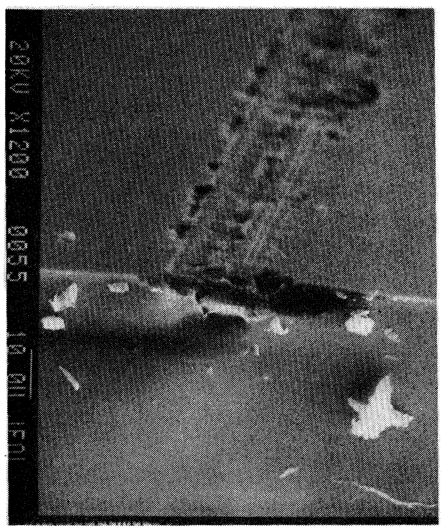

FIG. 5. Scanning electron microscope image of a scribed channel in silicon. Here a wafer was fractured perpendicular to a scratch and the image was taken at an angle of 75° from the normal to the planar surface.

Figure 6 shows a schematic diagram of the arrangement of the scribed channels and bolometers for the periodic ($\mathcal{P}$) arrays; the thinner lines are the channels and the heavier lines with the circular contact pads at each end represent the driver-detector strips. Aluminum was used for all strips in this experiment so that any strip could be used interchangeably as a driver or detector. The pair of Al strips with a single channel located adjacent to the array was placed there to allow for the measurement of the third-sound velocity on smooth silicon C_s outside of the array and to permit the measurement of third-sound pulse reflections from a single channel, as described earlier. Two of these adjacent patterns were created so that the arrays would be symmetric, but only one pair of strips was actually used for C_s and reflection measurements. Each array contained 100 channels, each 2.9-cm long, arranged over 5 cm placed with lattice spacing $l = 500$ μm; on the quasiperiodic array, to be discussed later, the channel positions were chosen according to the Fibonacci sequence. Optical and SEM examination of the scratches revealed that they had width $S = 16 \pm 0.6$ μm with well-defined edges which were interrupted in places by small depressions which extended somewhat beyond the edges of the channels (see Fig. 5). The error in placement of the channels was less than 5 μm, which is less than 1% of the 500 μm spacing on the periodic array; the periodic array was therefore weakly disordered spatially.

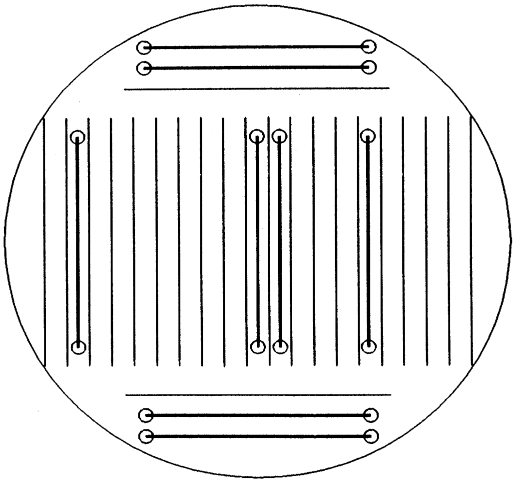

FIG. 6. Schematic view of a periodic array of scribed channels in silicon. The view is to scale except that each array contains 100 parallel channels; here only 20 are shown for clarity. The Al driver-detector strips are shown with the round contact pads attached. The driver-detector pair located adjacent to the main array is to allow measurement of the third-sound velocity on smooth silicon and to measure the reflection from a single scratch at various times during the array measurements.

Four Al bolometers were placed within each array at the positions shown in Fig. 6. For identification, they will be referred to, from left to right, as $\mathcal{P}1$–$\mathcal{P}4$. Bolometer $\mathcal{P}2$ was located at the center of the array. The spacing between the first and second bolometer strip on each array was 2.10 cm, between the second and third was 0.25 cm, and between the third and fourth was 1.00 cm. The strips were 2.1-cm long by 150-μm wide by 30-nm thick. Because of problems encountered when attaching leads to the contact pads on smooth[25] silicon, it was necessary to make contact with Ag pins supported above each wafer and held against the contact pads with BeCu spring clips. A small drop of silver paint was used between each pin and pad to improve electrical contact.

IV. RESULTS AND ANALYSIS

The data presented in this section were taken on a periodic array $\mathcal{P}$ by driving with a continous sine wave at $\mathcal{P}3$ and detecting with either $\mathcal{P}2$ or $\mathcal{P}4$ using the electronics shown in Fig. 2. The standard notation used for designating the driver and detector will be "$\mathcal{P}m$-$\mathcal{P}n$," where "m" designates the driver and "n" designates the detector. The $\mathcal{P}3$-$\mathcal{P}2$ spacing was $5l$, or five times the lattice spacing, whereas the $\mathcal{P}3$-$\mathcal{P}4$ spacing was $20l$. The third-sound amplitude as a function of frequency was measured by sweeping the cw drive frequency over a broad range, typically from ~10 Hz to 50 kHz. As mentioned previously, because the third-sound drive is thermal, the third-sound frequency excited is twice the applied sine-wave frequency. All frequencies reported below are *third-sound* frequencies.

Figure 7 shows the magnitude of the received third-sound (in arbitrary units) on the periodic array as a function of third-sound frequency f (drive, $f/2$) for 12 increasing values of the film thickness using $\mathcal{P}3$ as the driver and $\mathcal{P}2$ as the detector ($\mathcal{P}3$-$\mathcal{P}2$ sweeps). The dashed line on each trace indicates zero-received amplitude. Several features of the frequency traces are worth noting. First, the average amplitude of the detected signal, neglecting the detailed structure of each trace, drops with increasing frequency. It will be shown later that this is an attenuation property of third-sound propagation on smooth silicon; it is seen on wafers containing no scatterers. Second, there is structure to the data which evolves and becomes more pronounced with increasing film thickness (decreasing C_s). Except for the thinnest coverages, that structure includes ranges of frequency (gaps) where essentially no third-sound amplitude is detected. Third, the observed structure appears to scale in frequency roughly as C_s, with prominent features moving to lower frequencies as C_s decreases. (Note that the frequency range decreases for each successive section of Fig. 7.)

To check this scaling with C_s, the data can be plotted as a function of f/C_s, the third-sound wave vector on the smooth silicon; this is shown in Fig. 8(a) for four thicknesses. Key features generally occur at fixed values of f/C_s; the peaks at $f/C_s=10$ and 20 cm^{-1} correspond to third-sound wavelength values, λ, in registry with the scatterers, i.e., $\lambda=2l$ and l, respectively. This structure

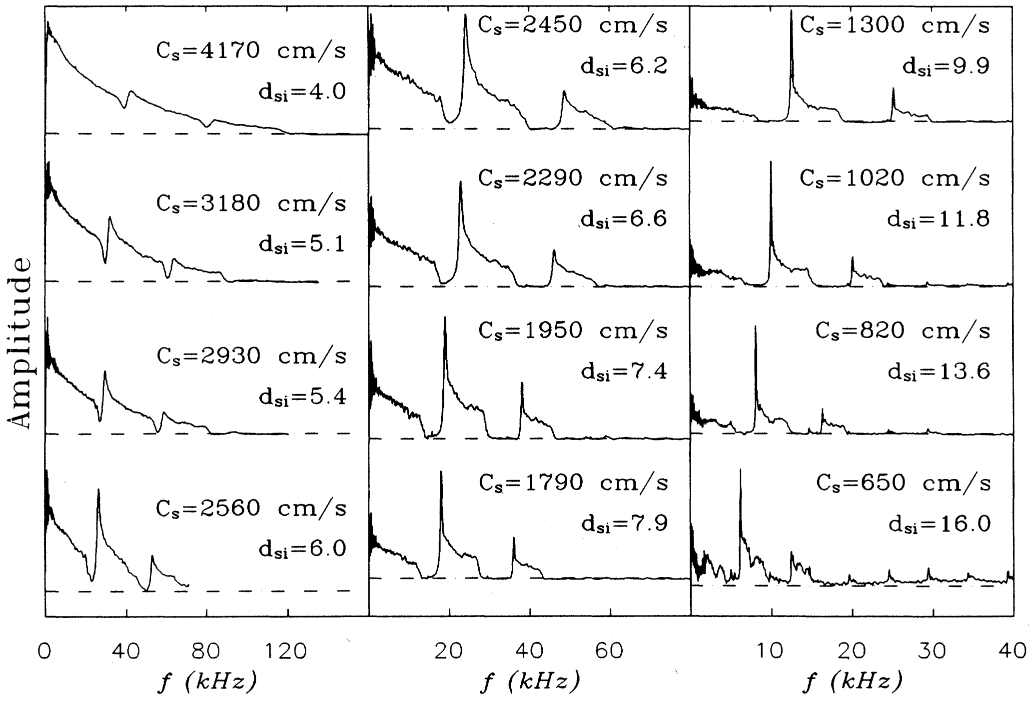

FIG. 7. Received third-sound signal at detector $\mathcal{P}2$ with cw third-sound drive at driver $\mathcal{P}3$ located $5l$ away. The data are shown as a function of the third-sound frequency for a sequence of film thickness values. Clear bands and gaps are present. Note that the frequency scale changes for different panels in the figure.

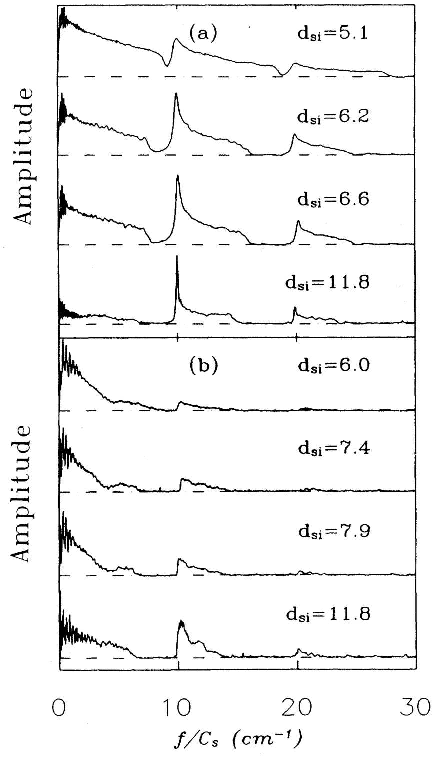

FIG. 8. Received third-sound signal as a function of third-sound wave vector for selected values of the helium film thickness driver-detector separations of (a) 5*l* and (b) 20*l*.

as a function of wave vector is the band structure of the classical periodic system, directly analogous to the band structure observed for electrons in a periodic potential.[26] There are bands in frequency where the detected amplitude is strong, and gaps where the amplitude is either greatly reduced or, at higher film coverages, zero.

It is clear from the data that the gaps become wider at higher coverages; the relationship between gap width and helium film thickness will be discussed shortly. The absence of bands above the third is believed to be due primarily to the finite width of the Al driver-detector strips. For values of $f/C_s \simeq 30$ cm^{-1}, the third-sound wavelength is twice the width of the Al strips; for shorter wavelengths, the strips quickly become very inefficient at driving and detecting third sound. The numerous small features visible at much higher frequencies (particularly for $d_{si} = 16.0$ layers in Fig. 7) are not third sound, but are vapor-sound ($C_v = 6840$ cm/s, $T = 1.35$ K) resonances set up between the silicon wafer and the plate above it used to support the contact pins for the Al strips.

In addition to driving with $\mathcal{P}3$ and detecting with $\mathcal{P}2$, experiments were also carried out by driving with $\mathcal{P}2$ and detecting with $\mathcal{P}3$; the $\mathcal{P}3$-$\mathcal{P}2$ and $\mathcal{P}2$-$\mathcal{P}3$ experiments resulted in very similar behavior. Data were also taken on the periodic array for a larger driver-detector separation by driving with $\mathcal{P}3$ and detecting with $\mathcal{P}4$. Those data, for four film thicknesses, are shown in Fig. 8(b). Here the drop in average amplitude with increasing frequency due to attenuation is even more pronounced than on the $\mathcal{P}3$-$\mathcal{P}2$ traces.

In Figs. 8(a) and 8(b), there is structure at low frequencies which might appear at first glance to be noise. Figures 9(a) and 9(b) show in detail the low-frequency data

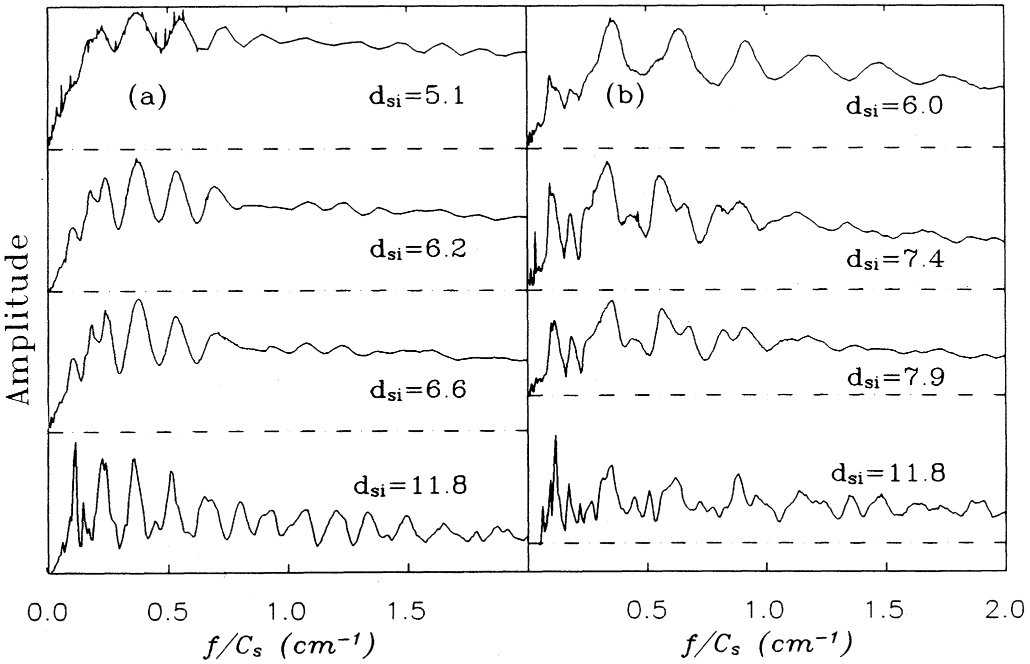

FIG. 9. Expanded view of the low wave-vector portion of the data shown in Fig. 8 for driver-detector separations (a) 5*l* and (b) 20*l*.

from the $\mathcal{P}3$-$\mathcal{P}2$ and $\mathcal{P}3$-$\mathcal{P}4$ sweeps of Figs. 8(a) and 8(b), respectively. The structure is not noise, but apparently well-defined modes with wavelengths in the range $0.5 \lesssim \lambda \lesssim 5$ cm. These low-frequency modes were present on all of the substrates studied. For a given film thickness the modes on the various substrates were generally the same but not precisely identical. We believe that these modes are modes of the wafer-holder system; the frequencies are of the order of those expected for a global drumhead third-sound mode on the wafer.

In the discussion of the data from the periodic array shown in Fig. 7, several qualitative features of the data were noted. The first was that, neglecting the detailed structure of the traces, the average detected amplitude drops with increasing frequency. To be certain that that behavior was not caused predominantly by the presence of scatterers, a silicon substrate $\mathcal{S}$ was prepared with four Al bolometers, denoted $\mathcal{S}1-\mathcal{S}4$, which were placed at the same positions on a wafer as $\mathcal{P}1-\mathcal{P}4$ were on the periodic array. The $\mathcal{S}$ substrate contained no scatterers; it was simply a smooth silicon wafer with four bolometers. Figures 10(a)–10(d) compare the results of $\mathcal{S}3$-$\mathcal{S}2$ sweeps to $\mathcal{P}3$-$\mathcal{P}2$ sweeps at four coverages. Similar data were taken on the smooth wafer using $\mathcal{S}3$ as driver and $\mathcal{S}4$ as detector. It is clear from this data that third sound on silicon at these temperatures (1.35 K) exhibits some frequency-dependent attenuation; the data on the smooth wafer are consistent with the "envelope" seen in the periodic data. Note that both ordinary third-sound attenuation and the efficiency of the bolometers are involved in the reduction of third-sound amplitude at the higher frequencies.

The most striking feature of the data from the periodic array is the appearance of bands and gaps in the frequency response of the system. As seen in Figs. 10(a)–10(d), the difference between the response seen on the smooth wafer and that seen on the periodic array depends on the film thickness; in Fig. 10(a), the periodic system differs markedly from the smooth system only when the third-sound wavelength is near an integer multiple of twice the lattice spacing, i.e., $\lambda = 2ml$ for integer m. As d increases, regions develop where the received third-sound amplitude is essentially zero; this occurs first between the second and third band, then, at higher coverages, between the first and second band. There is a second major feature of the data: the bands are observed to be strongly asymmetric. Next, we discuss each of these points in more detail.

The fact that the gaps widen with increasing helium film thickness implies that the channels become stronger scatterers at higher coverage, i.e., $n = C_s/C_r$ increases with d. The band structure can be used[27] to estimate the value of the index of refraction for the scatterers by calculating where the band edges should occur as a function of n and comparing those locations to the actual band-edge positions. This calculation corresponds to the Kronig-Penney analysis[26] of an electron in a one-dimensional periodic potential. The electron calculation considers a periodic square-well potential with electron wave vector $k = k_1$ where the potential is low ($V = 0$) and $k = k_2$ where the potential is high ($V = V_0$). If the $V = V_0$ regions of the potential are of width W and the periodicity of the lattice is l, the condition for allowed frequencies of wave propagation is

$$\cos(k_2 W)\cos[k_1(l - W)] - \left[\frac{k_2^2 + k_1^2}{2k_1 k_2}\right]\sin(k_2 W)\sin[k_1(l - W)] \le 1 , \quad (13)$$

with the band edges occurring where the equality holds. In the electron case, the wave vectors are related to the kinetic energy E_k of the electron by $\hbar k = \sqrt{2\mu E_k}$, where μ is the mass of the electron. For the case of classical waves, the wave vector is related to the velocity by $k_i = \omega / C_i$, where C_i is either C_s or C_r. Using this and the definition of the index of refraction, $n = C_s/C_r$, Eq. (13) can be rewritten as

$$1 \ge \frac{(1-u)}{2}\cos\left[\frac{\omega}{c_1}(l - nW)\right] + \frac{1+u}{2}\cos\left[\frac{\omega}{c_1}(l + nW)\right] , \quad (14)$$

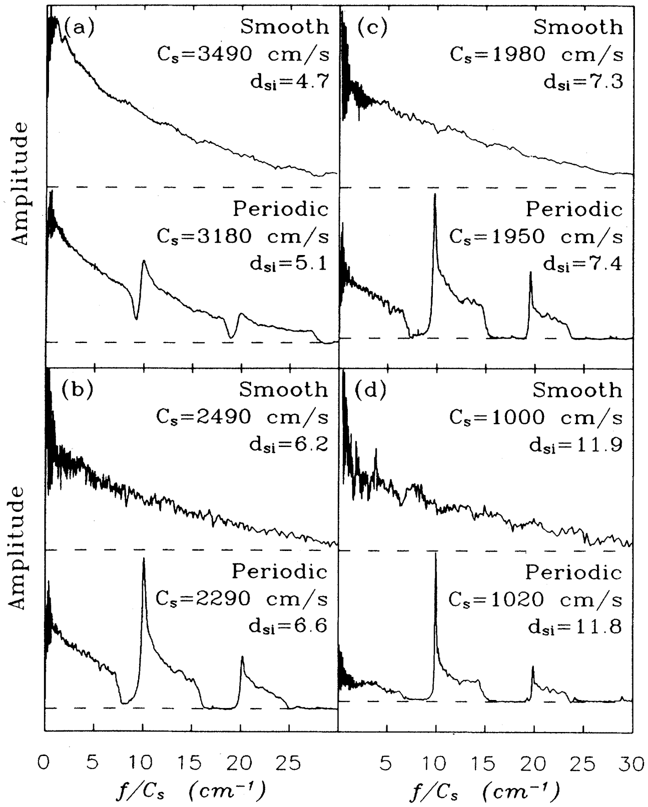

FIG. 10. Comparison of the received third-sound signal for the $\mathcal{P}2$-$\mathcal{P}3$ (periodic) and $\mathcal{S}2$-$\mathcal{S}3$ (smooth) substrates at a driver-detector separation of $5l$ as a function of third-sound wave vector for a selection of helium film thickness values. The film thickness values for each segment (a)–(d) of the figure are not identical since the data were taken at different times, but they are close enough to illustrate the point that there is ordinary third-sound present and that it is generally responsible for the broad decay of the signals with the wave vector.

where $\omega = k_1/c_1$ and $u \equiv (n+1/n)/2$. For given values of n, values of ω can be found such that the right-hand side of Eq. (14) equals 1; Fig. 11 (smooth lines from top to bottom) shows these values for $1 \leq n \leq 5$, plotted as f/C_s to facilitate comparison to the data, for the first three gaps. The measured value of the channel width, 16 μm, was used for W. The areas labeled "GAP" indicate those regions where the right-hand side of Eq. (14) is greater than one; waves with these wave vectors cannot propagate within the array. The evolution of the gap widths with increasing n is clear.

The results of the band calculation can now be used, with the data from the periodic array, to obtain the index of refraction for the channels at each value of film thickness. The technique is shown schematically in Fig. 11 for data at two coverages; the widths of the gaps in the data match the calculated widths for appropriate values of n. The results of such a procedure are shown for nine coverages in Fig. 12; error bars reflect the range in index resulting from the uncertainty in determining the positions of the gap edges.

Another technique, which can be used to estimate the strength of the channels as scatterers, involves measuring reflected pulses from a single channel, as described earlier. Single-cycle zero-offset clamped sine-wave pulses of various frequencies f ($f \equiv 1/$ pulse period) were directed at a single channel and the reflected pulse amplitude $A_{\text{reflected}}$ was compared to the incident amplitude A_{direct}. Using the same approach as that described above in the calculation of the band-gap widths, the reflection coefficient for a wave of frequency f incident on a single channel of width W can be calculated by matching boundary conditions at both edges of the channel for incident, reflected, and transmitted waves outside the channel with the wave components in the channel. The result is an expression for the reflected amplitude

$$R = \left[\frac{A_{\text{reflected}}}{A_{\text{direct}}}\right]^2 = \frac{\frac{1}{4}[n-(1/n)]^2 \sin^2(\omega W n/C_1)}{\cos^2(\omega W n/C_1) + \frac{1}{4}[n+(1/n)]^2 \sin^2(\omega W n/C_1)} . \tag{15}$$

Figure 13 shows the result of the calculation for reflected amplitude for several values of n (the x axis corresponds to $n=1$) along with observed reflection data at four film thicknesses; for $d<6$ layers, no reflected pulse was visible. This approach for determining n for the strips is not as reliable as using the positions of the band gaps; it depends strongly on knowing the frequency of the incident wave. The applied third-sound pulses were, of course, a superposition of an infinite number of frequencies, and because higher frequencies are attenuated more strongly than lower frequencies, pulses broaden as they travel and look progressively lower in frequency. This is the most reasonable explanation for the deviation of the data from the predictions for fixed values of n seen in Fig. 13 for $f/C_s > 7$ cm^{-1}. In spite of this difficulty at a higher frequency, the low-frequency results are in good qualitative agreement with what is obtained using the band structure. That is, the index is seen to be lower at the thinnest coverage ($n \sim 1.75$ at 6.2 layers) and essentially constant ($n \sim 3$) for the three highest coverages studied.

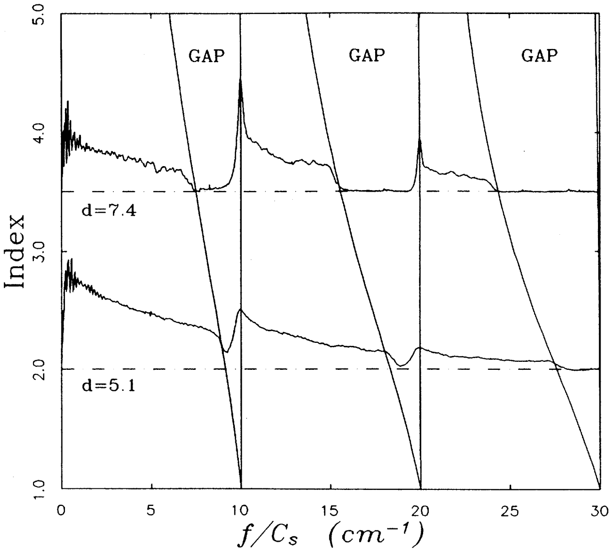

FIG. 11. Calculated gap edges (smooth curves) as a function of the index of refraction based on a Kronig-Penney–type analysis. Superimposed on the calculation are selections from the data for two different values of the helium film thickness to illustrate that it is possible to deduce the index of refraction from the data.

In addition to probing the periodic system with a continuous sine-wave drive, as described above, the response of the system to a train (tone burst) of four sine-wave cycles was also studied. The trains were driven at $\mathcal{P}3$ and

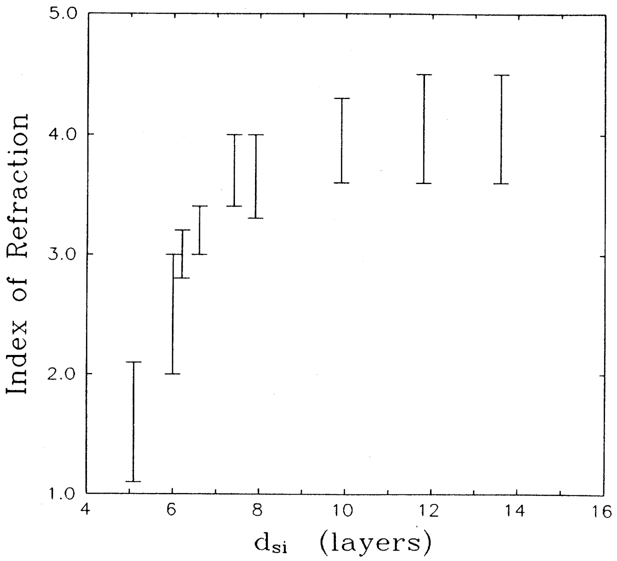

FIG. 12. Index of refraction values deduced from comparisons between the data and the Kronig-Penny calculation for the positions of the gap edges for various values of the helium film thickness.

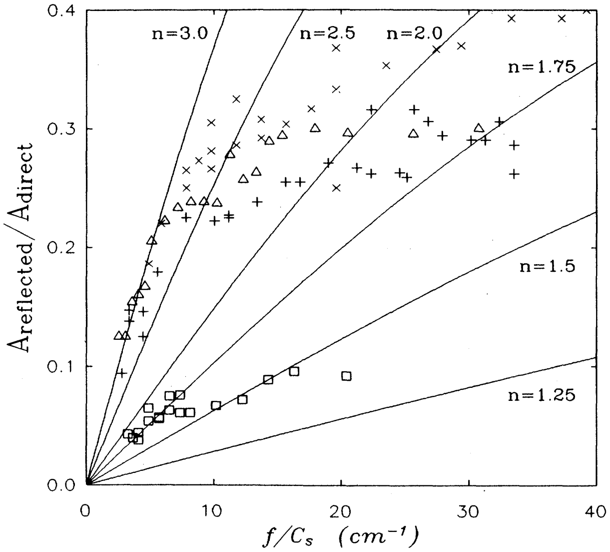

FIG. 13. The ratio of the reflected single-cycle sine-wave pulse height to the incident pulse height as a function of the third-sound wave-vector. The frequency is taken to be 1/(pulse width). Data are shown for four values of the helium film thickness (squares, $d=6.2$ layers; triangles, $d=7.4$ layers; pulses, $d=7.9$ layers; crosses, $d=11.8$ layers). The smooth curves are the theoretical values for the amplitude ratio for the various index of refraction values indicated.

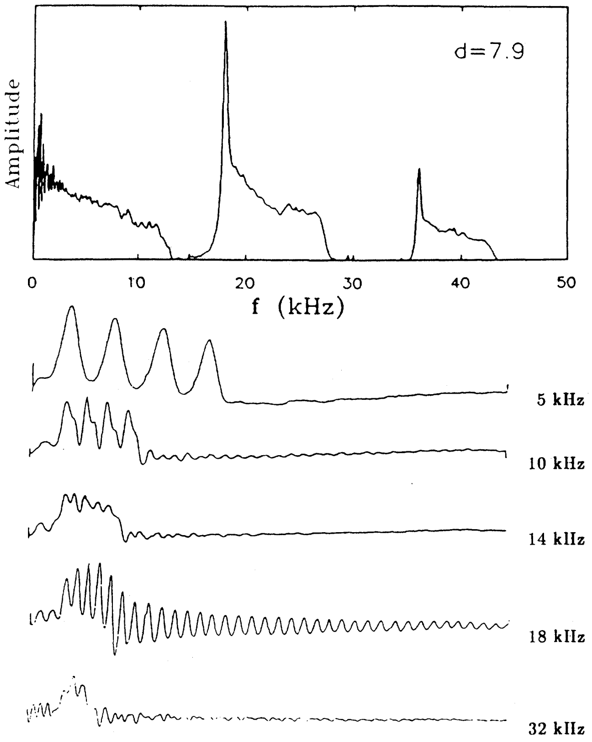

FIG. 14. Observed third-sound signals for an applied pulse train of four sine-wave cycles at five different frequencies chosen to illustrate the difference in the received signals for frequencies generated in the bands and in the gaps. The boxed part of the figure is the band structure for the helium film thickness used for all of the data in the figure. The lower data traces are the received third-sound amplitudes at $\mathcal{P}3$ as a function of time for a drive at $\mathcal{P}2$.

detected at $\mathcal{P}2$. The results for five frequencies are shown in Fig. 14. The response for 5 and 10 kHz, both in the first band, show the well-resolved pulse train arriving at the detector. At a frequency of 14 kHz, chosen because it lies in the first gap, lower-frequency components of the packet propagate reasonably well (as evidenced by the broad received signal), but the individual 14-kHz pulses are not cleanly visible. At 18 kHz, the peak of the second band, the system responds strongly, and in fact appears to resonate. At 32 kHz the frequency is again in a gap and individual pulses do not propagate well. This response of the system to wave packets of various predominant frequencies is taken as further evidence that the periodic structure shows the expected behavior.

In order to better understand the detailed structure of the bands observed on the periodic array, simulations were performed[28] which calculated the amplitude transmitted *through* an array of 20 one-dimensional scatterers with lattice spacing $l=500$ μm. Each element of the array consisted of a channel of width W and a smooth region of width $l-W$. The propagation of third sound across each unit was described by a 2×2 frequency-dependent matrix $T(\omega)$, where

$$T_{11}=T_{22}^{*}=(\cos\phi+ia\sin\phi)\exp^{i\theta}\ ,$$

$$T_{12}=T_{21}^{*}=ib\sin(\phi)\exp^{i\theta}\ ,$$

$\phi=\omega Wn/C_s$, $\theta=\omega(l-W)/C_s$, and a and b are amplitudes that depend on the index of refraction as $a=(n^2+1)/2n$ and $b=(n^2-1)/2n$. Transmission through m units was calculated by multiplying m matrices. The calculated transmitted amplitude for a 20-element array is shown in Fig. 15(a) as a function of f/C_s; for this computation $n=3.5$ and $C_s=2000$ cm/s.

The calculated transmission shown in Fig. 15(a) bears only limited resemblance to the third-sound data taken on the periodic array for a driver-detector spacing of 20 channels [Fig. 8(b)]. This suggests that the experimental array is not perfect. The simulation can be modified to include several perturbing effects which may be present in the experimental system. First, the frequency sweeps taken on the smooth silicon wafer [Figs. 10(a)–10(d)] indicate that there is some frequency-dependent attenuation present in these systems. This can be included in the simulation by including a factor of $\exp^{-\delta\omega}$ in the transmission matrix. A second effect which may be present in the periodic array is site disorder, a variation in the index of refraction from one channel to the next.[28] Site disorder would have a strong effect on the modes at the high-frequency edge of each band, as these modes have antinodes on the channels; modes at the low-frequency edge of each band have nodes on the channels, and are much less sensitive to variations in the strength of the scattering from the channels.

The effect of attenuation and site disorder are shown

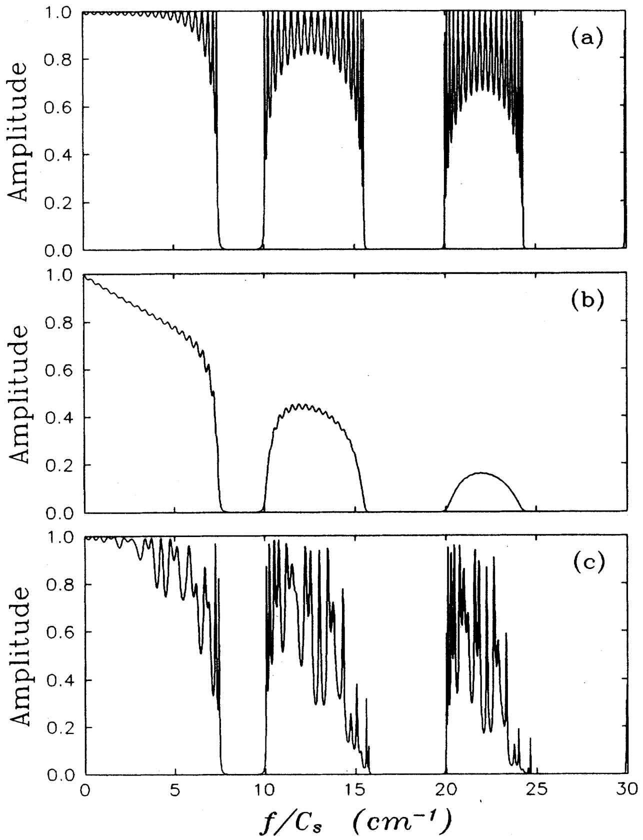

FIG. 15. Simulated transmitted amplitudes for transmission through an array of 20 elements for the case of $n=3.5$ and $C_s=2000$ cm/s. (a) Perfect periodic array, (b) attenuation present of the form $\exp^{-\delta\omega}$ with $\delta=2.5\times10^5$/s, and (c) site disorder (but no attenuation) present with $n=3.5+\delta n$, where n is selected at random for the various elements of the array from the range $-1\leq\delta n\leq1$.

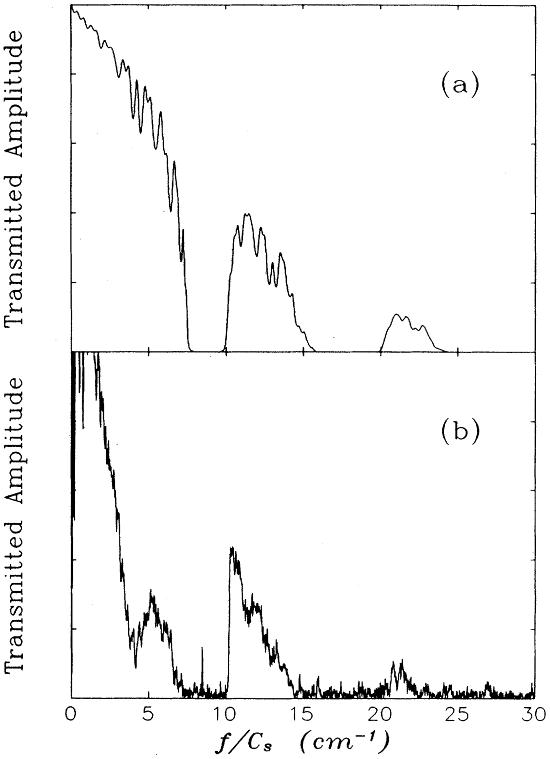

FIG. 16. (a) Simulated transmitted amplitude for a 20-element periodic array. The simulation includes *both* the attenuation and the site disorder described in Fig. 15. (b) Experimental periodic data for a driver-detector spacing of $20l$.

separately in Figs. 15(b) and 15(c), respectively, for a 20-scatterer array with $C_s=2000$ cm/s and $l=500$ μm. Figure 15(b) uses $n=3.5$ and $\delta=2.5\times10^5$ s^{-1}, which results in a transmitted amplitude through the array which is attenuated by a factor of $1/e$ from its dc value at $f/C_s\simeq20$ cm^{-1}. Note that although the drop in transmitted amplitude with increasing frequency is similar to what is seen in the data, the bands which result from the calculation are quite symmetric and do not show the detailed structure observed in the data. Figure 15c, on the other hand, *does not include attenuation,* but instead shows the effect of introducing site disorder by choosing the index for each scatterer at random in the range $2.5\leq n\leq4.5$; that is, $n=3.5+\Delta n$, where Δn is chosen at random for each scatterer from the range $-1\leq\Delta n\leq1$. The result of this calculation has several qualitative features in common with the periodic array data. First, the bands are no longer symmetric; the site disorder has affected the high-frequency modes in each band more strongly than the low-frequency modes, as expected. Second, the bands show more structure as a result of the site disorder, and in this respect are somewhat more like the data in Fig. 8(b). Unlike the data, however, the average amplitude from one band to the next does not diminish significantly, as is seen in the data and the simulation with attenuation.

Figure 16 shows the result of combining both attenuation ($\delta=2.5\times10^5$ s^{-1}) and site disorder ($-1\leq\Delta n\leq1$) in the simulation, and compares the result to data taken on the periodic array for a driver-detector spacing of 20 channels [the $d=7.4$ layer data from Fig. 8(b)]. It can be seen that the simulation accurately describes the qualitative, and to some extent the quantitative, features seen in the data, and it seems reasonable to conclude that both attenuation and site disorder are present in this system.

A substrate was also made which contained 100 scatterers distributed over 5 cm in a quasiperiodic configuration. The positions of the scatterers x_q were determined using the relation $x_q=q+T^{-1}[\mathrm{Int}(qT^{-1})]$, where q is an integer and $T^{-1}=(\sqrt{5}-1)/2$. This algorithm generates the Fibonacci sequence which is quasiperiodic because, although it is not periodic, it is also not random; it can be written as the sum of periodic functions.

When the quasiperiodic array was made, a new periodic array was also made, and these two substrates were mounted in the sample cell and run at 1.35 K. Figure 17 shows periodic and quasiperiodic data taken at four in-

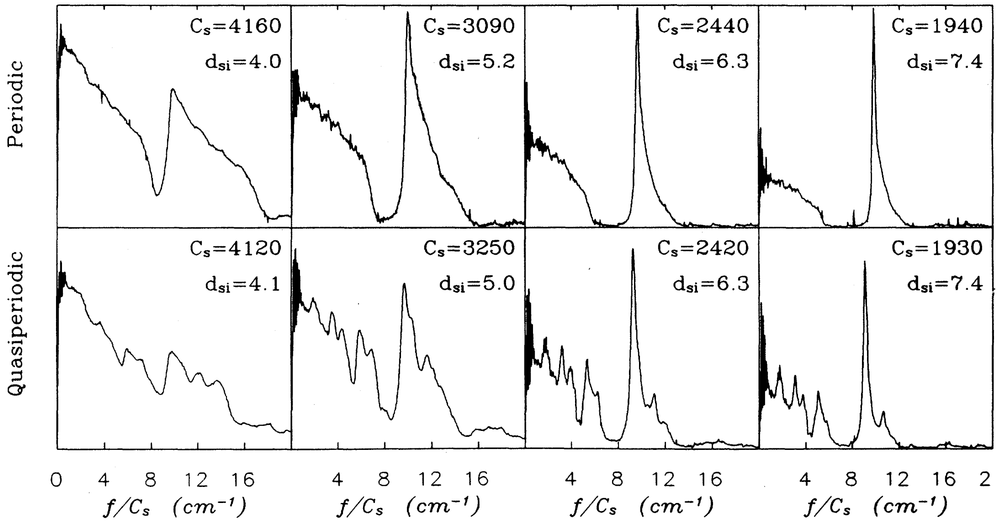

FIG. 17. Comparison of periodic and quasiperiodic third-sound amplitudes as a function of frequency for four selected values of the helium film thickness. The periodic array used for the data shown here was different from that used for the data presented earlier in this work.

creasing values of film thickness. The periodic data taken by driving with $\mathcal{P}2$ and detecting with $\mathcal{P}3$; the quasiperiodic data were taken by driving the $\mathcal{F}2$ and detecting with $\mathcal{F}3$. This periodic array displayed many features in common with that discussed earlier, but the details of the channels were clearly a bit different. The overall structure seen on the quasiperiodic array (Table I) is reminiscent of the new periodic data, but the quasiperiodicity has introduced substantially more structure, and the gap between the first and second bands has been weakened considerably. These effects are in qualitative agreement with predictions for a quasiperiodic array made by Sokoloff[29] and predictions for optical systems made by Kohmoto *et al.*[30]

The propagation of third sound through a quasiperiodic array can be simulated using the same matrix multiplication technique used in the analysis of the periodic array. The result of such a simulation for a 20-element

TABLE I. Channel locations—quasiperiodic array. Below is a listing of the channel locations for the quasiperiodic array, scaled over a range $0 < x \leq 1$, followed by the relative locations of the bolometer strips. To convert these coordinates to actual positions within the array, multiply by 5 cm.

No.	*x*	No.	*x*	No.	*x*	No.	*x*	No.	*x*
1	0.0073	21	0.2064	41	0.4100	61	0.6091	81	0.8127
2	0.0190	22	0.2181	42	0.4172	62	0.6208	82	0.8199
3	0.0263	23	0.2299	43	0.4290	63	0.6281	83	0.8317
4	0.0380	24	0.2371	44	0.4407	64	0.6398	84	0.8389
5	0.0498	25	0.2489	45	0.4480	65	0.6516	85	0.8507
6	0.0570	26	0.2606	46	0.4597	66	0.6588	86	0.8624
7	0.0688	27	0.2679	47	0.4715	67	0.6706	87	0.8697
8	0.0761	28	0.2796	48	0.4787	68	0.6823	88	0.8814
9	0.0878	29	0.2869	49	0.4905	69	0.6896	89	0.8932
10	0.0996	30	0.2987	50	0.4978	70	0.7014	90	0.9005
11	0.1068	31	0.3104	51	0.5095	71	0.7086	91	0.9122
12	0.1186	32	0.3177	52	0.5213	72	0.7204	92	0.9195
13	0.1303	33	0.3294	53	0.5285	73	0.7321	93	0.9312
14	0.1376	34	0.3412	54	0.5403	74	0.7394	94	0.9430
15	0.1493	35	0.3484	55	0.5475	75	0.7511	95	0.9502
16	0.1566	36	0.3602	56	0.5593	76	0.7584	96	0.9620
17	0.1683	37	0.3674	57	0.5710	77	0.7701	97	0.9693
18	0.1801	38	0.3792	58	0.5783	78	0.7819	98	0.9810
19	0.1874	39	0.3909	59	0.5901	79	0.7892	99	0.9928
20	0.1991	40	0.3982	60	0.6018	80	0.8009	100	1.0000
*F*1	0.2642	*F*2	0.4642	*F*3	0.5142	*F*4	0.6142		

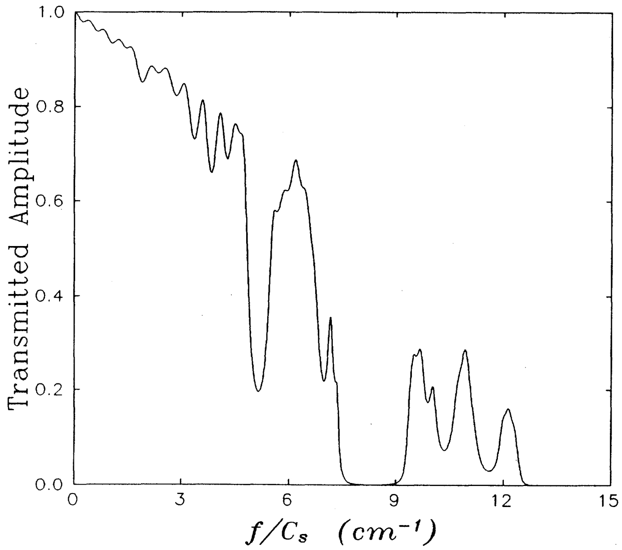

FIG. 18. Simulated transmitted amplitude through a 20-element quasiperiodic array for the case of both attenuation and site disorder present. Attenuation was of the form exp$^{-\delta\omega}$ with $\delta=2.5\times10^5$/s. Site disorder was of the form $n=3.5+\delta n$ with n selected at random for the various elements of the array from the range $-1\leq\delta n\leq1$.

quasiperiodic array, with the same attenuation ($\delta=2.5\times10^5$/s) and site disorder ($n=3.5+\Delta n$, $-1\leq\Delta n\leq1$) as were used in the earlier simulations, is shown in Fig. 18. The simulated transmission, calculated for $C_s=2000$ cm/s, is qualitatively quite similar to the quasiperiodic data in Fig. 17; considerably more structure is observed in both the simulated and observed quasiperiodic transmission than is seen in the periodic data.

V. SUMMARY

We have reported on a new experimental system useful for the study of the propagation of waves in the presence of scattering sites. Helium films offer unique advantages for such studies. The scattering strength of the scattering sites can be varied by means of simple changes in the helium film thickness. Results for periodic arrays of such sites reveal bands and gaps as expected for a periodic array. Nonideal features are observed and explained as due to imperfections in the periodic nature of the arrays. It should be straightforward to extend studies of this type to the case of two dimensions. In particular, integrated circuit technology techniques will be useful in preparing more uniform and precisely positioned scattering sites.

ACKNOWLEDGMENTS

We are indebted to R. Verner of the Physics and Astronomy machine shops for his suggestions and skill in the preparation of the patterned substrates. K. McCall and R. A. Guyer provided important advice and computer simulations which were used in the analysis of some of the data. We have benefitted from conversations with J. Machta, C. Condat, and P. Sheng. This work was supported by the National Science Foundation through Grant No. DMR 85-17939 and to a lesser extent through Grant No. DMR 88-20517.

---

[*] Current address: National Institute of Standards and Technology, Gaithersburg, MD 20899.

[†] Current address: Alcan International Ltd., Kingston, Ontario, Canada.

[1] See, for example, L. Brillouin, *Wave Propagation in Periodic Structures* (McGraw-Hill, New York, 1946).

[2] P. W. Anderson, Phys. Rev. **109**, 1492 (1958).

[3] See, for example, S. Putterman, *Superfluid Hydrodynamics* (North-Holland, Amsterdam, 1974).

[4] A brief account of some of the work we report here has been presented earlier: D. T. Smith, C. P. Lorenson, R. B. Hallock, K. McCall, and R. A. Guyer, Phys. Rev. Lett. **61**, 1286 (1988).

[5] D. T. Smith, C. P. Lorenson, and R. B. Hallock, Phys. Rev. B **40**, 6648 (1989).

[6] F. London, Nature **141**, 643 (1938).

[7] A more detailed analysis was developed by Lifshitz: E. M. Lifshitz, Zh. Eksp. Teor. Fiz. **29**, 94 (1955) [Sov. Phys.—JETP **2**, 73 (1956)]; and by Dzyaloshinski, Lifshitz, and Pitaevskii: I. E. Dzyaloshinskii, E. M. Lifshitz, and L. P. Pitaevskii, Adv. Phys. **10**, 165 (1961). The Lifshitz result reduces to that of London and of Casimir and Polder: H. B. G. Casimir and D. Polder, Phys. Rev. **73**, 360 (1948). The work of Sabisky and Anderson [E. S. Sabisky and C. H. Anderson, Phys. Rev. A **7**, 790 (1973)] is consistent with Eqs. (1) and (2).

[8] K. R. Atkins, Phys. Rev. **113**, 962 (1959).

[9] C. W. F. Everitt, K. R. Atkins, and A. Denenstein, Phys. Rev. **136**, A1494 (1964).

[10] J. S. Brooks, F. M. Ellis, and R. B. Hallock, Phys. Rev. Lett. **40**, 240 (1978).

[11] D. J. Bergmann, Phys. Rev. **188**, 370 (1969); Phys. Rev. A **3**, 2058 (1971).

[12] J. H. Scholtz, E. O. McLean, and I. Rudnick, Phys. Rev. Lett. **32**, 147 (1974); see also, I. Rudnick, *New Directions in Physical Acoustics Corso LXIII* (Societe Italiana di Fisica, Bologna, Italy, 1976), p. 112.

[13] R. K. Galkiewicz, K. L. Telschow, and R. B. Hallock, J. Low Temp. Phys. **26**, 147 (1977).

[14] M. W. Cole and E. Vittoratos, J. Low Temp. Phys. **22**, 223 (1976).

[15] E. R. Generazio and R. W. Reed, J. Low Temp. Phys. **56**, 355 (1984).

[16] W. F. Saam and M. W. Cole, Phys. Rev. B **11**, 1086 (1975).

[17] D. T. Smith and R. B. Hallock, Phys. Rev. B **34**, 226 (1986).

[18] D. T. Smith, M. Liebl, M. D. Bummer, and R. B. Hallock, in *Proceedings of the XVII International Conference on Low Temperature Physics,* edited by V. EcKern *et al.* (North-

Holland, Amsterdam, 1984).

[19] M. Z. Shoushtari and K. L. Telschow, Phys. Rev. B **26**, 4917 (1982).

[20] S. M. Cohen, R. A. Guyer, and J. M. Machta, Phys. Rev. B **33**, 4664 (1986).

[21] See Ref. 17 and D. T. Smith, K. M. Godshalk, and R. B. Hallock, Phys. Rev. B **36**, 202 (1987).

[22] MKS Instruments, Burlington, MA 01803.

[23] We attempted this same procedure on borosilicate glass and Pyrex. In the case of borosilicate glass, the scratches produced were not stable; they were susceptible to degradation in time—material along the edges of the scratches continued to flake off for many hours after the scratches were made. Pyrex was better in this regard, but it also was unacceptable due to pits in the surface of the glass we received from the vendor.

[24] The film thickness values reported in this work have been determined by use of the assumed van der Waals constants for silicon and glass of 36 and 27 $(\text{layers})^3$ K, respectively.

[25] Although silver paint remained firmly attached to etched silicon (Ref. 17) through thermal cycles, it was unreliable for the case of silicon with a smooth surface. The more complicated attachment procedure described in the text resolved this difficulty.

[26] See, for example, N. W. Ashcroft and N. D. Mermin, *Solid State Physics* (Saunders, Philadelphia, 1976).

[27] K. McCall and R. A. Guyer (private communication).

[28] This was first done by McCall and Guyer: K. McCall and R. A. Guyer, Bull Am. Phys. Soc. **33**, 806 (1988).

[29] J. Sokoloff (private communication).

[30] M. Kohmoto, B. Sutherland, and K. Iguchi, Phys. Rev. Lett. **58**, 2436 (1987).

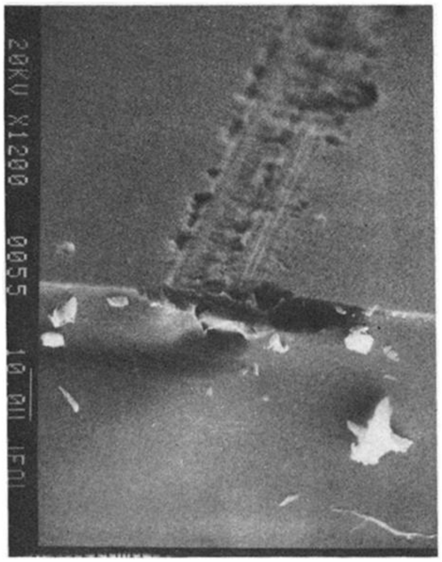

FIG. 5. Scanning electron microscope image of a scribed channel in silicon. Here a wafer was fractured perpendicular to a scratch and the image was taken at an angle of 75° from the normal to the planar surface.